

# Proton spin polarizabilities from polarized Compton scattering

B. Pasquini

*Dipartimento di Fisica Nucleare e Teorica, Università di Pavia, and  
Istituto Nazionale di Fisica Nucleare, Sezione di Pavia, I-27100 Pavia, Italy*

D. Drechsel

*Institut für Kernphysik, Johannes Gutenberg Universität, D-55099 Mainz, Germany*

M. Vanderhaeghen

*Physics Department, College of William and Mary, Williamsburg, VA 23187, USA, and  
Theory Center, Thomas Jefferson National Accelerator Facility, Newport News, VA 23606, USA*

(Dated: June 7, 2018)

Polarized Compton scattering off the proton is studied within the framework of subtracted dispersion relations for photon energies up to 300 MeV. As a guideline for forthcoming experiments, we focus the attention on the role of the proton's spin polarizabilities and investigate the most favorable conditions to extract them with a minimum of model dependence. We conclude that a complete separation of the four spin polarizabilities is possible, at photon energies between threshold and the  $\Delta(1232)$  region, provided one can achieve polarization measurements with an accuracy of a few percent.

PACS numbers: 13.60.Fz, 11.55.Fv, 14.20.Dh, 13.40.-f

## I. INTRODUCTION

The polarizabilities of a composite system such as the nucleon are elementary structure constants, just as its size and shape. They can be studied by applying electromagnetic fields to the system. The physical content of the nucleon polarizabilities can be visualized best by effective multipole interactions for the coupling of the electric ( $\vec{E}$ ) and magnetic ( $\vec{H}$ ) fields of a photon with the internal structure of the nucleon. This structure can be accessed experimentally by the Compton scattering process  $\gamma + N \rightarrow \gamma + N$  on the nucleon, see Refs. [1, 2] for recent reviews. When expanding the Compton scattering amplitude in the

energy of the photon, the zeroth and first order terms follow from a low energy theorem and can be expressed solely in terms of the charge, mass, and anomalous magnetic moment of the nucleon. The second order terms in the photon energy describe the response of the nucleon's internal structure to an electric or magnetic dipole field, they are given by the following effective interaction :

$$H_{\text{eff}}^{(2)} = -4\pi \left[ \frac{1}{2} \alpha_{E1} \vec{E}^2 + \frac{1}{2} \beta_{M1} \vec{H}^2 \right], \quad (1)$$

where the proportionality coefficients are the electric ( $\alpha_{E1}$ ) and magnetic ( $\beta_{M1}$ ) dipole (scalar) polarizabilities, respectively. These global structure coefficients are proportional to the electric and magnetic dipole moments of the nucleon which are induced when placing the nucleon in static electric and magnetic fields. They have been measured extensively using unpolarized Compton scattering. A fit to all modern low-energy Compton scattering data yields the following results for the proton [3]:

$$\begin{aligned} \alpha_{E1}^p &= [12.1 \pm 0.3(\text{stat}) \mp 0.4(\text{syst}) \pm 0.3(\text{mod})] \times 10^{-4} \text{ fm}^3, \\ \beta_{M1}^p &= [1.6 \pm 0.4(\text{stat}) \pm 0.4(\text{syst}) \pm 0.4(\text{mod})] \times 10^{-4} \text{ fm}^3, \end{aligned} \quad (2)$$

with the statistical, systematical and model-dependent errors, respectively. These values confirm, beyond any doubt, the dominance of the electric polarizability  $\alpha_{E1}$ . The tiny value of the magnetic polarizability,  $\beta_{M1}$ , comes about due to a cancellation of the large paramagnetic contribution of the  $N \rightarrow \Delta$  spin-flip transition with a nearly equally large diamagnetic contribution, partly due to pion loop effects.

The internal spin structure of the nucleon appears at third order in an expansion of the Compton scattering amplitude. It is described by the effective interaction

$$\begin{aligned} H_{\text{eff}}^{(3)} &= -4\pi \left[ \frac{1}{2} \gamma_{E1E1} \vec{\sigma} \cdot (\vec{E} \times \dot{\vec{E}}) + \frac{1}{2} \gamma_{M1M1} \vec{\sigma} \cdot (\vec{H} \times \dot{\vec{H}}) \right. \\ &\quad \left. - \gamma_{M1E2} E_{ij} \sigma_i H_j + \gamma_{E1M2} H_{ij} \sigma_i E_j \right], \end{aligned} \quad (3)$$

which involves one derivative of the fields with regard to either time or space :  $\dot{\vec{E}} = \partial_t \vec{E}$  and  $E_{ij} = \frac{1}{2}(\nabla_i E_j + \nabla_j E_i)$ , respectively. The four spin (or vector) polarizabilities  $\gamma_{E1E1}$ ,  $\gamma_{M1M1}$ ,  $\gamma_{M1E2}$ , and  $\gamma_{E1M2}$  describing the nucleon spin response at third order, can be related to a multipole expansion [4], as is reflected in the subscript notation. For example,  $\gamma_{M1E2}$  corresponds to the excitation of the nucleon by an electric quadrupole ( $E2$ ) field and its de-excitation by a magnetic dipole ( $M1$ ) field. Expanding the Compton scattering amplitude

to higher orders in the energy, one obtains higher order polarizabilities to the respective order, e.g., the quadrupole polarizabilities to fourth order [4, 5].

The effective Hamiltonians of Eqs. (1) and (3) describe a shift in the nucleon energies at second order in the electromagnetic fields. This has been implemented in recent years as a tool to calculate nucleon polarizabilities in lattice QCD. By calculating the mass shifts in a constant background field, and isolating the quadratic response, it has thus been possible to compute the electric polarizability of the neutron and other neutral octet and decuplet baryons [6], and the magnetic polarizability of the proton, neutron, and all other particles in the lowest baryon octet and decuplet states [7]. In Ref. [7],  $\beta_{M1}^p$  has been calculated by use of the Wilson action in the pion mass range  $0.5 \leq m_\pi \leq 1$  GeV and neglecting disconnected loop diagrams. For the smallest calculated pion mass of  $m_\pi \simeq 500$  MeV, a value of  $\beta_{M1}^p = (2.36 \pm 1.20) \times 10^{-4} \text{ fm}^3$  was obtained. While it is encouraging to see that the lattice result is in the right ballpark when compared to the experimental value of Eq. (2), a more precise comparison clearly requires a dynamical fermion calculation, including disconnected loop diagrams and much smaller pion masses. Such small pion masses would then allow one to extrapolate safely to the physical pion mass within the framework of chiral perturbation theory.

To determine the spin polarizabilities, Eq. (3) can likewise be used to calculate energy shifts of a polarized nucleon in an external field. As an example, consider a nucleon polarized along the  $z$ -axis and apply a magnetic field rotating with angular frequency  $\omega$  in the  $xy$  plane,

$$\vec{H} = B_0 [\cos(\omega t) \hat{e}_x + \sin(\omega t) \hat{e}_y], \quad (4)$$

where  $\hat{e}_i$  stands for the unit vector in the direction  $i = x, y$  and  $B_0$  is the magnitude of the field. Such a field leads to an energy shift  $\Delta E = \mp 2\pi\gamma_{M1M1}\omega B_0^2$  if the nucleon spin is oriented along the positive ( $-$ ) or negative ( $+$ )  $z$ -axis. The split between the two levels is then directly proportional to the magnetic dipole spin polarizability  $\gamma_{M1M1}$ .

It has been shown in Ref. [8] that allowing for background fields with suitable variations in space and time, lattice QCD should be able to calculate all six dipole polarizabilities. In particular, calculations are in progress to determine the electric polarizability of a charged particle such as the proton as well as the four proton spin polarizabilities of Eq. (3) [9].

A microscopic understanding of the nucleon's polarizabilities requires to quantify the interplay between resonance contributions, e.g., the  $N \rightarrow \Delta$  transition, and long range

pion cloud effects. Such systematic studies of the pion cloud effects became possible with the development of chiral perturbation theory (ChPT), by systematically expanding the lagrangian in the external momenta and the pion mass (“ $p$ -expansion”). The first such calculation to the one-loop order, at  $\mathcal{O}(p^3)$ , yielded the following leading terms for the proton scalar polarizabilities [10]:

$$\alpha_{E1}^p = 10\beta_{M1}^p = \frac{5\alpha_{em}g_A^2}{96\pi f_\pi^2 m_\pi} = 12.2, \quad (5)$$

where  $\alpha_{em} = 1/137$ ,  $g_A \simeq 1.27$ , and  $f_\pi = 92.4$  MeV. This result is in remarkable agreement with the experimental result of Eq. (2). It also illustrates that these quantities diverge in the chiral limit, which is a challenge for the lattice QCD calculations. Conversely, if one is in the “small  $m_\pi$ ” regime where the chiral expansion converges well, ChPT can complement the lattice calculations by extrapolating to the physical pion mass. The ChPT work was extended to  $\mathcal{O}(p^4)$  within the heavy-baryon expansion [11]. However, the agreement with the experimental values of the scalar polarizabilities became much more challenging when including the  $\Delta$  degree of freedom, which yields a large contribution to  $\beta_{M1}^p$  [12, 13, 14].

The spin polarizabilities have been calculated within the framework of ChPT at  $\mathcal{O}(p^3)$  [15] and  $\mathcal{O}(p^4)$  [16, 17, 18]. However, much less is known about these observables on the experimental side, except for the forward ( $\gamma_0$ ) and backward ( $\gamma_\pi$ ) spin polarizabilities of the proton, given by the following linear combinations of the polarizabilities of Eq. (3):

$$\gamma_0 = -\gamma_{E1E1} - \gamma_{M1M1} - \gamma_{E1M2} - \gamma_{M1E2}, \quad (6)$$

$$\gamma_\pi = -\gamma_{E1E1} + \gamma_{M1M1} - \gamma_{E1M2} + \gamma_{M1E2}. \quad (7)$$

The forward spin polarizability has been determined from the Gerasimov-Drell-Hearn sum rule experiments at MAMI and ELSA [19, 20],

$$\gamma_0 = (-1.00 \pm 0.08 \pm 0.10) \times 10^{-4} \text{ fm}^4, \quad (8)$$

and the recent experimental value for the backward spin polarizability has been obtained by a dispersive analysis of backward angle Compton scattering [2],

$$\gamma_\pi = (-38.7 \pm 1.8) \times 10^{-4} \text{ fm}^4. \quad (9)$$

No data exist for the other two independent proton spin polarizabilities. It is the aim of the present work to show that polarized Compton scattering, both near pion threshold and in

the  $\Delta(1232)$  resonance region, can be used to determine the remaining two spin polarizabilities.

The extraction of polarizabilities from Compton scattering data has been performed by three techniques. The first one is a low energy expansion of the Compton cross sections. Unfortunately this procedure is only applicable at photon energies well below 100 MeV, which makes a precise extraction a rather challenging task. The sensitivity to the polarizabilities is increased by measuring Compton scattering observables around pion threshold and into the  $\Delta(1232)$  resonance region. A second formalism which has been successfully applied to Compton data in this energy region makes use of dispersion relations. This formalism has been worked out for both unsubtracted [21] and subtracted [22] dispersion relations, and yield the values of the scalar polarizabilities given in Eq. (2). Recently, a third approach has been developed within the framework of a chiral effective field theory [23, 24, 25, 26]. For energies below and around pion threshold the full Compton scattering process has been calculated to fourth order in the small momenta, allowing for an independent extraction of the polarizabilities from Compton scattering data. The thus obtained values for  $\alpha_{E1}^p$  and  $\beta_{M1}^p$  in the work of [23, 25] are nicely compatible with the results given by Eq. (2).

In this work we study the polarized proton Compton scattering observables both below pion threshold and in the  $\Delta(1232)$  resonance region within the subtracted dispersion relation formalism of Ref. [22]. In particular we investigate the sensitivity of different beam and beam-target polarization observables to the extraction of the proton spin polarizabilities.

After a brief review of fixed- $t$  dispersion relations for the Compton scattering process in Section 2, we discuss different single and double polarization observables in Section 3. We present our results for these different polarization observables in Section 4 and study the sensitivity to the extraction of the proton spin polarizabilities. Finally, we give our conclusions in Section 5.

## II. FIXED-T SUBTRACTED DISPERSION RELATIONS

In this section we review the essentials of the dispersion relation formalism for real Compton scattering (RCS), a more detailed presentation can be found in Refs. [1, 22]. Let us first define the kinematics of RCS on the proton, the reaction

$$\gamma(q) + p(p) \rightarrow \gamma(q') + p(p'), \quad (10)$$

where the variables in brackets denote the four-momenta of the participating particles. The familiar Mandelstam variables are

$$s = (q + p)^2, \quad t = (q - q')^2, \quad u = (q - p')^2, \quad (11)$$

which are constrained by  $s + t + u = 2M^2$ , where  $M$  is the nucleon mass. The crossing-symmetric variable  $\nu$  is defined by

$$\nu = \frac{s - u}{4M}. \quad (12)$$

The two Lorentz invariant variables  $\nu$  and  $t$  are related to the initial ( $E_\gamma$ ) and final ( $E'_\gamma$ ) photon lab energies and to the lab scattering angle  $\theta_{\text{lab}}$  by

$$\begin{aligned} \nu &= E_\gamma + \frac{t}{4M} = \frac{1}{2}(E_\gamma + E'_\gamma), \\ t &= -4E_\gamma E'_\gamma \sin^2(\theta_{\text{lab}}/2) = -2M(E_\gamma - E'_\gamma). \end{aligned}$$

The  $T$  matrix of real Compton scattering can be expressed by 6 independent structure functions  $A_i(\nu, t)$ ,  $i = 1, \dots, 6$ , which were first introduced in Ref. [21]. These structure functions depend on  $\nu$  and  $t$ , they are free of kinematic singularities and constraints, and because of the crossing symmetry they satisfy the relation  $A_i(\nu, t) = A_i(-\nu, t)$ . Assuming further analyticity and an appropriate high-energy behavior, the amplitudes  $A_i$  fulfill unsubtracted dispersion relations (DRs) at fixed  $t$ ,

$$\text{Re}A_i(\nu, t) = A_i^B(\nu, t) + \frac{2}{\pi} \mathcal{P} \int_{\nu_{\text{thr}}}^{+\infty} d\nu' \frac{\nu' \text{Im}_s A_i(\nu', t)}{\nu'^2 - \nu^2}, \quad (13)$$

where  $A_i^B$  are the nucleon pole contributions of the Born terms describing the photon scattering off a point-like nucleon with anomalous magnetic moment, as explicitly given in App. A of Ref. [21]. Furthermore,  $\text{Im}_s A_i$  are the discontinuities across the  $s$ -channel cut of the Compton process, starting at pion production threshold, i.e.,  $\nu_{\text{thr}} = m_\pi + (m_\pi^2 + t/2)/(2M)$ , with  $m_\pi$  the pion mass. However, as can be deduced from the asymptotic behavior of the functions  $A_i(\nu, t)$  for  $\nu \rightarrow \infty$  and fixed  $t$  [22], such unsubtracted DRs do not converge for the amplitudes  $A_1$  and  $A_2$ . We therefore subtract the fixed- $t$  DRs of Eq. (13) at  $\nu = 0$ , with the result

$$\text{Re}A_i(\nu, t) = A_i^B(\nu, t) + [A_i(0, t) - A_i^B(0, t)] + \frac{2}{\pi} \nu^2 \mathcal{P} \int_{\nu_{\text{thr}}}^{+\infty} d\nu' \frac{\text{Im}_s A_i(\nu', t)}{\nu' (\nu'^2 - \nu^2)}. \quad (14)$$

Because of the two additional powers of  $\nu'$  in the denominator, these subtracted DRs should now converge for all of the invariant amplitudes.

The 6 subtraction functions  $A_i(\nu = 0, t)$  appearing in Eq. (14) can be determined by once-subtracted DRs in the variable  $t$ :

$$A_i(0, t) - A_i^B(0, t) = [A_i(0, 0) - A_i^B(0, 0)] + [A_i^{t-pole}(0, t) - A_i^{t-pole}(0, 0)] \\ + \frac{t}{\pi} \int_{4m_\pi^2}^{+\infty} dt' \frac{\text{Im}_t A_i(0, t')}{t'(t'-t)} + \frac{t}{\pi} \int_{-\infty}^{-2m_\pi^2 - 4Mm_\pi} dt' \frac{\text{Im}_t A_i(0, t')}{t'(t'-t)}, \quad (15)$$

where  $A_i^{t-pole}(0, t)$  represents the contribution of the poles in the  $t$  channel, in particular of the  $\pi^0$  pole in the case of  $A_2$  as explicitly evaluated in Ref. [22], and the subtraction constants  $a_i = A_i(0, 0) - A_i^B(0, 0)$  are related to the polarizabilities as explained below.

In order to evaluate the dispersion integrals in Eq. (14), the imaginary parts in the  $s$ -channel are calculated from the unitarity relation, taking into account the  $\pi N$  intermediate states and the resonant contributions of inelastic channels involving more pions in the intermediate states. In particular, for the  $\gamma N \rightarrow \pi N \rightarrow \gamma N$  contribution we use the multipole amplitudes from the analysis of Hanstein *et al.* [27] for energies  $\nu \leq 500$  MeV, and at the higher energies up to  $\nu = 1.5$  GeV we take the solutions of the SAID analysis [28]. The multi-pion intermediate states are approximated by the inelastic decay channels of the  $\pi N$  resonances as detailed in Ref. [22]. This simple approximation of the higher inelastic channels is quite sufficient, because these channels are largely suppressed by the energy denominator  $\nu'(\nu'^2 - \nu^2)$  in the subtracted DRs of Eq. (14).

The imaginary part in the  $t$ -channel integral from  $4m_\pi^2 \rightarrow +\infty$  in Eq. (15) is saturated by the possible intermediate states for the  $t$ -channel process, which lead to cuts along the positive  $t$ -axis. For values of  $t$  below the  $K\bar{K}$  threshold, the  $t$ -channel discontinuity is dominated by the two-pion intermediate states,  $\gamma\gamma \rightarrow \pi\pi \rightarrow N\bar{N}$ . We calculate this contribution by evaluating a unitarized amplitude for the  $\gamma\gamma \rightarrow \pi\pi$  subprocess, and then combine it with the  $\pi\pi \rightarrow N\bar{N}$  amplitudes as determined from dispersion theory by analytical continuation of the  $\pi N$  scattering amplitudes [29]. The second integral in Eq. (15) extends from  $-\infty$  to  $-2m_\pi^2 - 4Mm_\pi \approx -0.56$  GeV<sup>2</sup>. As long as we stay at small (negative) values of  $t$ , this integral is strongly suppressed by the denominator  $t'(t'-t)$  in Eq. (15), and therefore it can be approximated by the contributions of  $\Delta$ -resonance and non-resonant  $\pi N$  intermediate states. The latter contributions are evaluated by first evaluating the imaginary parts of the Compton amplitude in the physical  $s$ -channel region by unitarity, and then extrapolating these results into the unphysical region at  $\nu = 0$  and negative  $t$  by means of analytical continuation.

The 6 subtraction constants  $a_i$  in Eq. (15) are related to the electric ( $\alpha_{E1}$ ) and magnetic ( $\beta_{M1}$ ) scalar polarizabilities in the spin-independent sector,

$$\alpha_{E1} = -\frac{1}{4\pi}(a_1 + a_3 + a_6), \quad \beta_{M1} = \frac{1}{4\pi}(a_1 - a_3 - a_6), \quad (16)$$

and to the 4 spin-dependent or vector polarizabilities,

$$\begin{aligned} \gamma_{E1E1} &= \frac{1}{8\pi M}(a_2 - a_4 + 2a_5 + a_6), & \gamma_{M1M1} &= -\frac{1}{8\pi M}(a_2 + a_4 + 2a_5 - a_6), \\ \gamma_{E1M2} &= \frac{1}{8\pi M}(a_2 - a_4 - a_6), & \gamma_{M1E2} &= -\frac{1}{8\pi M}(a_2 + a_4 + a_6). \end{aligned} \quad (17)$$

Although in principle all 6 subtraction constants  $a_1$  to  $a_6$  could be used as fit parameters, we restrict the fit to the parameters  $a_5$  and  $a_6$ , or equivalently to the two spin polarizabilities  $\gamma_{E1E1}$  and  $\gamma_{M1M1}$ . For fixed values of the fit parameters  $a_5$  and  $a_6$ , the subtraction constants  $a_1$  and  $a_3$  are then determined by a recent global fit of the scalar polarizabilities to the low-energy data [3],

$$\begin{aligned} \alpha_{E1} + \beta_{M1} &= (13.8 \pm 0.4) \times 10^{-4} \text{ fm}^3, \\ \alpha_{E1} - \beta_{M1} &= (10.5 \pm 0.9 \text{ (stat. + syst.)} \pm 0.7 \text{ (mod.)}) \times 10^{-4} \text{ fm}^3. \end{aligned} \quad (18)$$

In the spin-dependent sector, we use the experimental values of the forward ( $\gamma_0$ ) and backward ( $\gamma_\pi$ ) spin polarizabilities describing the Compton spin-flip amplitude at  $\theta = 0^\circ$  and  $180^\circ$ , respectively. These observables have been expressed in Eqs. (6) and (7) by linear combinations of the polarizabilities defined in Eq. (17), they are related to the subtraction constants as follows:

$$\gamma_\pi = -\frac{1}{2\pi M}(a_2 + a_5), \quad \gamma_0 = \frac{1}{2\pi M}a_4. \quad (19)$$

In particular, the subtraction constant  $a_2$  is fixed by the value of  $\gamma_\pi$  given by Eq. (9). This definition of the backward spin polarizability includes both the dispersive and the large  $\pi^0$ -pole contribution. In the analysis of Ref. [2], the latter takes the value  $\gamma_\pi^{\pi^0\text{-pole}} = -46.7 \times 10^{-4} \text{ fm}^4$ , which leads to  $\gamma_\pi^{\text{disp}} = (8.0 \pm 1.8) \times 10^{-4} \text{ fm}^4$ . In fact, the pion pole contribution is not known to that accuracy, and therefore the error in Eq. (9) stems from both the dispersive and the pole contributions to the backward spin polarizability. The value of the forward spin polarizability, or equivalently of  $a_4$ , is fixed by Eq. (8). We conclude that the choice of the subtraction constants  $a_5$  and  $a_6$  as fit parameters is equivalent to varying the polarizabilities  $\gamma_{E1E1}$  and  $\gamma_{M1M1}$ . As can be seen from Eqs. (17) and (8), another possibility would be to fit  $a_2$  and  $a_6$  or  $\gamma_{E1M2}$  and  $\gamma_{M1E2}$ .



### III. CROSS SECTIONS AND ASYMMETRIES - FORMALISM

The general formalism for RCS with one or two polarized particles has been originally derived in Ref. [4]. In the following we only review some pertinent formulas necessary to define the observables for polarized incident photons scattered by polarized target nucleons.

We work in a reference frame with the  $z$  axis along  $\hat{q}$  (the direction of the incoming photon), the  $x$  axis in the scattering plane and in the half-plane of the outgoing photon, and the  $y$  axis perpendicular to the scattering plane along the direction  $(\hat{q} \times \hat{q}')$ . The photon-polarization density matrix is defined by the Stokes parameters  $\xi_i$  ( $i = 1, 2, 3$ ) as follows [30]:

$$\langle \varepsilon_\alpha \varepsilon_\beta^* \rangle = \frac{1}{2} (1 + \vec{\sigma} \cdot \vec{\xi})_{\alpha\beta} = \frac{1}{2} \begin{pmatrix} 1 + \xi_3 & \xi_1 - i\xi_2 \\ \xi_1 + i\xi_2 & 1 - \xi_3 \end{pmatrix}_{\alpha\beta}, \quad (20)$$

where  $\varepsilon^\mu$  is the photon polarization vector chosen in the radiation gauge,  $\vec{\varepsilon} \cdot \vec{q} = 0$ , and  $\alpha, \beta = 1, 2$  denote either of the two orthogonal directions  $x$  and  $y$ . The total degree of photon polarization is given by  $\xi = \sqrt{\xi_1^2 + \xi_2^2 + \xi_3^2}$ , and  $\xi_\ell = \sqrt{\xi_1^2 + \xi_3^2}$  and  $\xi_2$  describe the degrees of linear and circular polarization, respectively. Furthermore,  $\xi_2 = +1$  and  $\xi_2 = -1$  correspond to right- and left-handed states, respectively, and in the case of linear polarization the azimuthal angle  $\phi$  between the electric field and the scattering plane is defined by  $\cos 2\phi = \xi_3/\xi_\ell$  and  $\sin 2\phi = \xi_1/\xi_\ell$ . With these definitions, the Stokes parameters take the same value in the c.m. and lab frames.

The nucleon polarization density matrix is described by a polarization four-vector  $S^\mu$  that is orthogonal to the nucleon four-momentum [30],

$$\langle u(p)\bar{u}(p) \rangle = \frac{1}{2} (\gamma \cdot p + M) (1 + \gamma_5 \gamma \cdot S), \quad (21)$$

where  $u(p)$  is a nucleon Dirac spinor normalized as  $\bar{u}(p)u(p) = 2M$ .

The differential cross section is related to the  $T$ -matrix by

$$\frac{d\sigma}{d\Omega} = \Phi^2 |T|^2, \quad \text{with} \quad \Phi = \begin{cases} \frac{1}{8\pi M} \frac{E'_\gamma}{E_\gamma} & \text{(lab frame)} \\ \frac{1}{8\pi\sqrt{s}} & \text{(c.m. frame)}. \end{cases} \quad (22)$$

The  $T$ -matrix for polarized photons and polarized targets can be decomposed in 8 independent functions  $W_{ij}$ ,

$$|T(\vec{\gamma}\vec{N} \rightarrow \gamma N)|^2 = W_{00} + W_{03}\xi_3 + N \cdot S (W_{30} + W_{33}^+\xi_3)$$

$$+ K \cdot S (W_{11}^+ \xi_1 + W_{12}^+ \xi_2) + Q \cdot S (W_{21}^+ \xi_1 + W_{22}^+ \xi_2), \quad (23)$$

with the orthogonal four-vectors  $K$ ,  $N$ , and  $Q$  defined as

$$K_\mu = \frac{1}{2}(q' + q)_\mu, \quad N_\mu = \epsilon_{\mu\alpha\beta\gamma} P'^\alpha Q^\beta K^\gamma, \quad Q_\mu = \frac{1}{2}(p - p')_\mu = \frac{1}{2}(q' - q)_\mu, \quad (24)$$

where  $\epsilon_{0123} = 1$ . The photon asymmetry  $\Sigma$  follows if the nucleon polarization vector is set to zero, and the unpolarized case  $|T|^2 = W_{00}$  is recovered for vanishing photon and nucleon polarization vectors.

In terms of the invariant amplitudes  $A_i$ , the functions  $W_{ij}$  read [4, 31]:

$$\begin{aligned} W_{00} = & \frac{1}{4}(4M^2 - t)(t^2|A_1|^2 + \eta^2|A_3|^2) - \frac{1}{4}(t^3|A_2|^2 - \eta^3|A_4|^2) \\ & - \nu^2 t (t + 8\nu^2)|A_5|^2 + \frac{1}{2}\eta(t^2 + 2M^2\eta)|A_6|^2 \\ & + \text{Re}\{2\nu^2 t^2(A_1 + A_2)A_5^* + \frac{1}{2}\eta^2(4M^2 A_3 + tA_4)A_6^*\}, \end{aligned} \quad (25)$$

$$W_{03} = \frac{\eta t}{2} \text{Re}\{((4M^2 - t)A_1 + 4\nu^2 A_5)A_3^* + 4M^2 A_1 A_6^*\}, \quad (26)$$

$$W_{30} = -8\nu \text{Im}(tA_1 A_5^* + \eta A_3 A_6^*), \quad (27)$$

$$\begin{aligned} W_{33}^\pm = & \text{Im}\{-8\nu [(tA_1 - (t + 4\nu^2)A_5)A_6^* + \eta A_3 A_5^*] \\ & \pm \frac{2}{m}(tA_2 - 4\nu^2 A_5)(\eta A_4^* + tA_6^*)\}, \end{aligned} \quad (28)$$

$$\begin{aligned} W_{11}^\pm = & \text{Im}\left\{\frac{t}{2M}((4M^2 - t)A_1 + 4\nu^2 A_5)(\eta A_4^* + tA_6^*)\right. \\ & \left. \pm 2\nu t (tA_2 - 4\nu^2 A_5)A_6^*\right\}, \end{aligned} \quad (29)$$

$$\begin{aligned} W_{12}^\pm = & \text{Re}\left\{-\frac{\eta}{2M}((4M^2 - t)A_3 + 4M^2 A_6)(\eta A_4^* + tA_6^*)\right. \\ & \left. \pm 2\nu t (tA_2 - 4\nu^2 A_5)A_5^*\right\}, \end{aligned} \quad (30)$$

$$\begin{aligned} W_{21}^\pm = & 2\text{Im}\left\{-M(tA_2 - 4\nu^2 A_5)(\eta A_3^* + (t + 4\nu^2)A_6^*)\right. \\ & \left. \pm \nu(tA_1 - (t + 4\nu^2)A_5)(\eta A_4^* + tA_6^*)\right\}, \end{aligned} \quad (31)$$

$$W_{22}^\pm = 2\text{Re}\left\{-Mt(tA_2 - 4\nu^2 A_5)A_1^* \mp \nu\eta A_3(\eta A_4^* + tA_6^*)\right\}, \quad (32)$$

where we have introduced the invariant variable  $\eta = 4\nu^2 + t - t^2/(4M^2)$ . Below the pion photoproduction threshold the functions  $A_i$  are real, and therefore only the 6 structures

$W_{00}, W_{03}, W_{12}^\pm$ , and  $W_{22}^\pm$  contribute below threshold.

In the following, we focus on the asymmetries that can be obtained by varying the photon and target polarizations in Eq. (23):

- circular photon polarization ( $\xi_2 = \pm 1$ ) and target spin aligned in the  $\pm z$  direction,

$$\Sigma_{2z} = \frac{\sigma_{+z}^R - \sigma_{+z}^L}{\sigma_{+z}^R + \sigma_{+z}^L} = \frac{\sigma_{+z}^R - \sigma_{-z}^R}{\sigma_{+z}^R + \sigma_{-z}^R} = \frac{C_z^K W_{12}^+ + C_z^Q W_{22}^+}{W_{00}}, \quad (33)$$

where the coefficients  $C_z^{K,Q}$  can be written in terms of lab or invariant variables as

$$\begin{aligned} C_z^K &= -\frac{1}{2}(E_\gamma + E'_\gamma \cos \theta_{\text{lab}}) = -\frac{s - M^2}{2M} - \frac{t(s + M^2)}{4M(s - M^2)}, \\ C_z^Q &= \frac{1}{2}(E_\gamma - E'_\gamma \cos \theta_{\text{lab}}) = -\frac{t(s + M^2)}{4M(s - M^2)}, \end{aligned} \quad (34)$$

- circular photon polarization ( $\xi_2 = \pm 1$ ) and target spin aligned in the  $\pm x$  directions,

$$\Sigma_{2x} = \frac{\sigma_{+x}^R - \sigma_{+x}^L}{\sigma_{+x}^R + \sigma_{+x}^L} = \frac{\sigma_{+x}^R - \sigma_{-x}^R}{\sigma_{+x}^R + \sigma_{-x}^R} = \frac{C_x^K W_{12}^+ + C_x^Q W_{22}^+}{W_{00}}, \quad (35)$$

with

$$C_x^K = C_x^Q = -\frac{1}{2} E'_\gamma \sin \theta_{\text{lab}} = -\frac{M\sqrt{-\eta t}}{2(s - M^2)}, \quad (36)$$

- linearly polarized photons, either parallel or perpendicular to the scattering plane ( $\xi_3 = \pm 1$ ), and target nucleon polarized perpendicularly to the scattering plane,

$$\Sigma_{3y} = \frac{(\sigma^\parallel - \sigma^\perp)_y - (\sigma^\parallel - \sigma^\perp)_{-y}}{(\sigma^\parallel + \sigma^\perp)_y + (\sigma^\parallel + \sigma^\perp)_{-y}} = C_y^N \frac{W_{33}^+}{W_{00}}, \quad (37)$$

with

$$C_y^N = \frac{M}{2} E_\gamma E'_\gamma \sin \theta_{\text{lab}} = \frac{M}{4} \sqrt{-\eta t}, \quad (38)$$

- linearly polarized photons, either parallel or perpendicular to the scattering plane ( $\xi_3 = \pm 1$ ), and unpolarized target nucleons,

$$\Sigma_3 = \frac{\sigma^\parallel - \sigma^\perp}{\sigma^\parallel + \sigma^\perp} = \frac{W_{03}}{W_{00}}, \quad (39)$$

- photons linearly polarized at  $\varphi = \pm\pi/4$  with respect to the scattering plane ( $\xi_1 = \pm 1$ ) and the nucleon target polarized in the scattering plane in the  $\pm z$  direction,

$$\Sigma_{1z} = \frac{\sigma_{+z}^{\pi/4} - \sigma_{+z}^{-\pi/4}}{\sigma_{+z}^{\pi/4} + \sigma_{+z}^{-\pi/4}} = \frac{\sigma_{+z}^{\pi/4} - \sigma_{-z}^{\pi/4}}{\sigma_{+z}^{\pi/4} + \sigma_{-z}^{\pi/4}} = \frac{C_z^K W_{11}^+ + C_z^Q W_{21}^+}{W_{00}}, \quad (40)$$

with coefficients  $C_z^{K,Q}$  as defined in Eqs. (34),

- photons linearly polarized at  $\varphi = \pm\pi/4$  with respect to the scattering plane ( $\xi_1 = \pm 1$ ) and nucleon targets polarized in the  $\pm x$  direction,

$$\Sigma_{1x} = \frac{\sigma_{+x}^{\pi/4} - \sigma_{+x}^{-\pi/4}}{\sigma_{+x}^{\pi/4} + \sigma_{+x}^{-\pi/4}} = \frac{\sigma_{+x}^{\pi/4} - \sigma_{-x}^{\pi/4}}{\sigma_{+x}^{\pi/4} + \sigma_{-x}^{\pi/4}} = \frac{C_x^K W_{11}^+ + C_x^Q W_{21}^+}{W_{00}}, \quad (41)$$

with  $C_x^{K,Q}$  given in Eq. (36).

#### IV. RESULTS AND DISCUSSION

In this section we present our predictions for the polarization observables. Our results are based on subtracted DRs evaluated with the pion photoproduction multipoles of Refs. [27, 28] as input. Because of the subtraction, two-pion and heavier intermediate states will generally yield only small corrections. Four of the subtraction constants are determined by the experimental values for the polarizabilities  $\alpha_{E1}, \beta_{M1}, \gamma_0$ , and  $\gamma_\pi$ . The remaining two constants are obtained by fixing the spin polarizabilities  $\gamma_{E1E1}$  and  $\gamma_{M1M1}$ . In the following figures, we start from the predictions of fixed- $t$  DRs for the dispersive part of the spin polarizabilities [1, 5],

$$\gamma_{E1E1} = -4.3 \times 10^{-4} \text{ fm}^4, \quad \gamma_{M1M1} = 2.9 \times 10^{-4} \text{ fm}^4, \quad (42)$$

which are then varied by  $\pm 2$  units. We note that here and in the following discussion including the figures, the values of the spin polarizabilities refer only to their dispersive parts, that is, the pion pole contribution,  $\gamma_{E1E1}^{\pi^0\text{-pole}} = -\gamma_{M1M1}^{\pi^0\text{-pole}} = 11.68 \times 10^{-4} \text{ fm}^4$ , has been subtracted. Because of the relatively large error bar for  $\gamma_\pi$ , we also vary this polarizability within its error band while keeping  $\gamma_{E1E1}$  and  $\gamma_{M1M1}$  fixed at their central values.

Figure 1 shows the asymmetry  $\Sigma_{2z}$ , with circular photon polarization and target aligned parallel to the incoming photon. We observe asymmetries up to 90 % and a strong dependence on both angle and energy, with distinct structures near the threshold for pion photoproduction. Although the asymmetry near  $\theta_{\text{lab}} = 90^\circ$  is smaller than for the forward and backward directions, it is rather sensitive to a variation of  $\gamma_{M1M1}$  both near threshold and in the  $\Delta$  (1232) resonance region. Within the range of the variation,  $\Sigma_{2z}$  changes by 15-20 %, which provides a promising signal to determine the spin polarizability  $\gamma_{M1M1}$ . The following Fig. 2 displays the same information for the asymmetry  $\Sigma_{2x}$ , with circular photon polarization and target aligned sideways to the incident photon. Contrary to the previous

figure, the maximum asymmetry is now reached at scattering angles  $\theta_{\text{lab}} \approx 90^\circ$ , and the maximum sensitivity occurs by changing  $\gamma_{E1E1}$ . Within the range of variation, this observable changes by 15 % near threshold and 40 % in the  $\Delta$  region. The right panels of Figs. 1 and 2 show that these observables are hardly changed by a variation of  $\gamma_\pi$ . As a result, the observables  $\Sigma_{2z}$  and  $\Sigma_{2x}$  sample conclusive and complementary information on the nucleon's spin structure. Furthermore, through the input of the DRs, they are related to the physics of the observables E and F of pion photoproduction.

The full angular distribution for  $\Sigma_{2z}$  and  $\Sigma_{2x}$  are shown in Fig. 3 for a photon beam of 240 MeV. It is seen that the discussed sensitivity extends over a large angular range between  $30^\circ$  and  $150^\circ$ . In view of the error bars of the backward scalar and vector polarizabilities,  $\alpha_{E1} - \beta_{M1}$  and  $\gamma_\pi$ , respectively, the cleanest information should however come from angles around  $\theta_{\text{lab}} \approx 90^\circ$ .

Figure 4 displays the results for the beam asymmetry  $\Sigma_3$ , for linear photon polarization, which is obtained by averaging the double-polarization observable  $\Sigma_{3y}$  over the target polarizations. This observable rises from large negative values at low energies to positive values in the resonance region. Moreover, there appear interesting cusp effects, especially at forward angles. The figure shows strong sensitivity to changes of  $\gamma_{M1M1}$ . Within the range of our variation, the asymmetry  $\Sigma_3$  changes by about 0.15 near threshold and nearly 0.30 in the resonance region. The LEGS data [32] taken at  $65^\circ$  and  $90^\circ$  are compatible with our central value for  $\gamma_{M1M1}$  (full lines), they scatter about this value at  $135^\circ$ . As in the previous examples, the variation of  $\gamma_\pi$  leads to much smaller effects. The following Fig. 5 shows the full angular distribution for  $\Sigma_3$  and the double-polarization observable  $\Sigma_{3y}$  in the resonance region. Large asymmetries are predicted for both observables over a wide angular range. Moreover, the sensitivity to the variation is large, and while  $\Sigma_3$  is particularly sensitive to  $\gamma_{M1M1}$ , the related double-polarization asymmetry  $\Sigma_{3y}$  changes strongly with  $\gamma_{E1E1}$ . We conclude that these two observables are particularly useful to disentangle the unknown spin polarizabilities.

The physics behind the asymmetry  $\Sigma_3$  is addressed in Fig. 6 as function of the photon energy. The Born terms, subtraction constants, and  $t$ -channel contributions provide a negative background whose height at the resonance depends strongly on the value of  $\gamma_{M1M1}$ . The S-wave multipoles in the dispersion integral provide the interesting cusp effect near threshold through the opening of the imaginary part, whereas the P-waves are responsible for the

further increase to large positive values in the  $\Delta(1232)$  resonance region. In conclusion, the large effect is mainly given by the  $M_{1+}^{(3/2)}$  multipole of pion photoproduction.

Let us now address the question of the model dependence of the dispersive approach. The general answer is that the errors in fixed- $t$  dispersion relations increase with both the beam energy and the scattering angle. If the energy gets larger, the unknown contributions of the higher resonances and backgrounds become more and more important for the evaluation of the  $s$ -channel dispersion integrals. Large angles and energies, on the other hand, require the knowledge of the subtraction functions at large (negative)  $t$ -values. Of course, the error also depends on the specific variable under discussion. We have studied these error sources for all the shown variables and found them to yield only small corrections in all the interesting cases, that is for large asymmetries and large sensitivity to the variation. Specifically for  $\Sigma_3$  and  $\Sigma_{3y}$  in Fig. 5, the neglect of the two-pion production changes these asymmetries by less than 0.01 at all energies and angles. It is therefore reasonable to assume that also the neglected higher resonance and background contributions above  $\nu = 1.5$  GeV are irrelevant for our discussion. Concerning the error from the  $t$ -channel integral, we find that the contribution from the negative  $t$ -channel cut is negligible for  $E_\gamma \leq 230$  MeV. At the energy  $E_\gamma = 275$  MeV shown in Fig. 5, the asymmetry  $\Sigma_3$  increases by less than 0.02 if we completely neglect that contribution, while  $\Sigma_{3y}$  is even less affected by the  $t$ -channel integral. In conclusion, even a very conservative estimate yields errors of a few percent at most, which are almost negligible in view of the large range of variation predicted for  $\Sigma_3$  and  $\Sigma_{3y}$ .

Let us finally discuss the beam-target asymmetries with photons linearly polarized at azimuthal angles  $\phi = \pm 45^\circ$  with respect to the scattering plane. These asymmetries are related to the observables G and H of pion photoproduction. They vanish below the one-pion threshold, because they thrive on the imaginary part of the scattering amplitudes. For the same reason, Fig. 7 does not show a peak near the  $\Delta$  resonance, because all  $\Delta$  multipoles carry the same phase. Instead, these observables are strongly enhanced by interference of non-resonant S-wave and resonant P-wave pion production. Since the pion photoproduction multipoles are quite well known in the  $\Delta$  region, we expect a rather model-independent information. The asymmetry  $\Sigma_{1z}$  turns out to be small at all angles and energies. Figure 7 shows the most promising kinematics at angles near  $\theta_{\text{lab}} = 90^\circ$ , where the asymmetry changes up to about 8 % over the range of variation. The asymmetry  $\Sigma_{1x}$ , on the other hand, has its

maximum sensitivity at the backward angles. However, the variations of  $\gamma_{E1E1}$  and  $\gamma_{M1M1}$  yield similar effects, such that the observed change is qualitatively proportional to the difference of the two polarizabilities. In conclusion, these asymmetries  $\Sigma_{1x}$  and  $\Sigma_{1z}$  would have to be measured with an accuracy of a few percent in order to get useful information on the spin polarizabilities.

## V. SUMMARY AND CONCLUSIONS

Compton scattering probes the response of the nucleon to an external electromagnetic field. At low energies, this response is described by 2 scalar and 4 vector polarizabilities, which contain global information on the excitation spectrum. Whereas the scalar polarizabilities are now known with relatively small error bars, our knowledge on the spin-dependent sector is as yet incomplete. Only two combinations of the vector polarizabilities have been measured. The forward spin polarizability has been determined by forward dispersion relations as an energy-weighted integral over the helicity-dependent total cross sections. Furthermore, the backward spin polarizability has recently been measured both below and in the  $\Delta(1232)$  resonance region, however with a larger model dependence. It has been known for some time that it will take a full-fledged experimental program including several polarization observables in order to achieve a complete separation of the spin polarizabilities. Considerable theoretical work has been dedicated to finding the appropriate observables and kinematics for this purpose.

In our present work we study polarized Compton scattering within the framework of dispersion relations at  $t=\text{const}$ . Subtraction of these relations speeds up the convergence of the dispersion integrals, and the subtraction constants of the 6 relativistic amplitudes turn out to be linear combinations of the 6 polarizabilities. In most cases also the unsubtracted integrals converge and hence a prediction for the polarizabilities is given. However, we choose to subtract all 6 integrals in order to reduce the model dependence on the high-energy spectrum as much as possible. Four of the subtraction constants are then fixed by the experimental values for the electric ( $\alpha_{E1}$ ) and magnetic ( $\beta_{M1}$ ) scalar polarizabilities as well as the forward ( $\gamma_0$ ) and backward ( $\gamma_\pi$ ) spin polarizabilities. The remaining two independent polarizabilities are taken to be  $\gamma_{E1E1}$  and  $\gamma_{M1M1}$ . They are varied about a central value as predicted by dispersion relations, within a range which comprises several predictions from effective field

theories and dispersive approaches.

Whereas the scalar polarizabilities contribute to the differential cross section already at second order in the photon beam energy, the vector polarizabilities appear only at third or fourth order, depending on the observable. It is therefore not surprising that it takes at least 100 MeV to get visible effects of the vector polarizabilities. Even at energies near the pion production threshold, the asymmetries change at most by 10 % over the range of our variation. Of course, the experiments could eventually yield polarizabilities far outside the range of the existing predictions. However we choose to stay on the conservative side regarding our predictions. Much larger effects are obtained in the first resonance region, in which both the cross sections and the asymmetries increase considerably. Specifically, we find a good chance to solve the open questions by the following two independent setups:

- Circularly polarized photons and targets aligned in the beam direction ( $\Sigma_{2z}$ ) or transverse to the beam in the scattering plane ( $\Sigma_{2x}$ ). Both asymmetries should yield a reasonably large sensitivity to the spin polarizabilities in the threshold region and increasingly large effects closer to the resonance region. Moreover, the response to the variation shows interesting cusp effects at threshold and a distinctly different sensitivity of these observables with regard to  $\gamma_{E1E1}$  and  $\gamma_{M1M1}$ .
- Linearly polarized photons, parallel or perpendicular to the scattering plane, and with unpolarized targets ( $\Sigma_3$ ) or with targets polarized perpendicular to the scattering plane ( $\Sigma_{3y}$ ). The sensitivity of these two observables is relatively small near threshold but very large in the resonance region. Moreover, the variations of the spin polarizabilities affect the observables in a completely different way, with  $\Sigma_3$  being mainly sensitive to  $\gamma_{M1M1}$  whereas  $\Sigma_{3y}$  being mainly sensitive to  $\gamma_{E1E1}$ .

We further looked at the observables  $\Sigma_{1z}$  and  $\Sigma_{1x}$ , obtained with photons linearly polarized at an angle of  $45^\circ$  against the scattering plane and target alignment perpendicular to this plane. However, these asymmetries turn out to be small in general, and even though the relative effect of the variations may be large, such experiments will require asymmetry measurements at the few percent level.

With the advent of new experimental tools as polarized targets and photon beams it will be possible to study the full spin structure of Compton scattering. The new HIGS project [33] of a high-intensity beam with circularly polarized photons in an energy range



up to 140-160 MeV is ideally suited to perform the discussed experiments in the threshold region. Complementary investigations should be performed at energies closer to the first resonance region, in which we expect much larger cross sections and sensitivities to the spin polarizabilities. Such experiments in the first resonance region are planned using the Crystal Ball detector at MAMI [34]. We strongly believe that only a combination of such experimental projects will provide the "sharp knife" to extract the spin polarizabilities in an unambiguous way. The spin polarizabilities of the nucleon are fundamental structure constants of the nucleon, just as shape and size of this strongly interacting many-body system, which strongly justifies the experimental effort. Such activities are both important and timely, they will provide stringent precision tests for the existing predictions of effective field theories and the new results expected from the lattice gauge community for the polarizability of the nucleon.

### Acknowledgments

The authors are grateful to J. Ahrens, R. Miskimen, and V. Pascalutsa for useful discussions. This research was supported by the Deutsche Forschungsgemeinschaft (SFB443), by the DOE grant DE-FG02-04ER41302 and DOE contract DE-AC05-06OR23177 under which Jefferson Science Associates operates the Jefferson Laboratory, and the EU Integrated Infrastructure Initiative Hadron Physics Project under contract number RII3-CT-2004-506078.

- 
- [1] D. Drechsel, B. Pasquini and M. Vanderhaeghen, Phys. Rept. **378**, 99 (2003).
  - [2] M. Schumacher, Prog. Part. Nucl. Phys. **55**, 567 (2005).
  - [3] V. Olmos de Leon *et al.*, Eur. Phys. J. A**10**, 207 (2001).
  - [4] D. Babusci, G. Giordano, and G. Matone, A.I. L'vov, Phys. Rev. **58**, 1013(1998).
  - [5] B. R. Holstein, D. Drechsel, B. Pasquini, and M. Vanderhaeghen, Phys. Rev. C **61**, 034316 (2000).
  - [6] J. Christensen, W. Wilcox, F. X. Lee, and L. M. Zhou, Phys. Rev. D **72**, 034503 (2005).
  - [7] F. X. Lee, L. Zhou, W. Wilcox, and J. Christensen, Phys. Rev. D **73**, 034503 (2006).
  - [8] W. Detmold, B. C. Tiburzi, and A. Walker-Loud, Phys. Rev. D **73**, 114505 (2006).

- [9] W. Detmold, A. Walker-Loud, and B. C. Tiburzi, arXiv:hep-lat/0610018.
- [10] V. Bernard, N. Kaiser, and Ulf-G. Meißner, Phys. Rev. Lett. **67**, 1515 (1991).
- [11] V. Bernard, N. Kaiser, A. Schmidt, and Ulf-G. Meißner, Phys. Lett. B **319**, 269 (1993); Z. Phys. A **348**, 317 (1994).
- [12] T.R. Hemmert, B.R. Holstein, and J. Kambor, Phys. Lett. B **395**, 89 (1997); Phys. Rev. D **55**, 5598 (1997).
- [13] T.R. Hemmert, B.R. Holstein, J. Kambor, and G. Knöchlein, Phys. Rev. D **57**, 5746 (1998).
- [14] V. Pascalutsa, Prog. Part. Nucl. Phys. **55**, 23 (2005).
- [15] V. Bernard, N. Kaiser, J. Kambor, and Ulf-G. Meißner, Int. J. Mod. Phys. E **4**, 193 (1995).
- [16] X. D. Ji, C. W. Kao, and J. Osborne, Phys. Rev. D **61**, 074003 (2000).
- [17] K. B. Vijaya Kumar, J. A. McGovern, and M. C. Birse, Phys. Lett. B **479**, 167 (2000).
- [18] G. C. Gellas, T. R. Hemmert, and Ulf-G. Meißner, Phys. Rev. Lett. **85**, 14 (2000).
- [19] J. Ahrens *et al.*, Phys. Rev. Lett. **87**, 022003 (2001).
- [20] H. Dutz *et al.*, Phys. Rev. Lett. **91**, 192001 (2003).
- [21] A.I. L'vov, V.A. Petrun'kin, and M. Schumacher, Phys. Rev. C **55**, 359 (1997).
- [22] D. Drechsel, M. Gorchtein, B. Pasquini, and M. Vanderhaeghen, Phys. Rev. C **61**, 015204 (2000).
- [23] S.R. Beane, M. Malheiro, J.A. McGovern, D.R. Phillips, and U. van Kolck, Nucl. Phys. A **747**, 311 (2005); Phys. Lett. B **567**, 200 (2003), Erratum-ibid. B **607**, 320 (2005).
- [24] V. Pascalutsa and D. R. Phillips, Phys. Rev. C **67**, 055202 (2003); Phys. Rev. C **68**, 055205 (2003).
- [25] R.P. Hildebrandt, H.W. Griesshammer, T.R. Hemmert, B. Pasquini, Eur. Phys. J. A **20**, 293 (2004).
- [26] R.P. Hildebrandt, H.W. Griesshammer, T.R. Hemmert, Eur. Phys. J. A **20**, 329 (2004).
- [27] O. Hanstein, D. Drechsel, and L. Tiator, Nucl. Phys. A **632**, 561 (1998).
- [28] R.A. Arndt, I.I. Strakovsky, and R.L. Workman, Phys. Rev. C **53**, 430 (1996).
- [29] G. Höhler, *Pion-Nucleon Scattering*, Landolt-Börnstein, Vol.I/9b2, ed. H. Schopper, Springer (1983).
- [30] V.B. Berestetskii, E.M. Lifshitz, and L.P. Pitaevskii, *Quantum Electrodynamics*, Pergamon Press (1982).
- [31] G.V. Frolov, ZhETP **39**, 1829 (1960) [Sov. Phys. JETP **12**, 1277 (1961)];

- M.G. Ryshkin and G.V. Frolov, *Yad. Fiz.* **13**, 1270 (1971) [*Sov. J. Nucl. Phys.* **13**, 731 (1971)].
- [32] G. Blanpied *et al.*, *Phys. Rev. C* **64**, 025203 (2001).
- [33] H.R. Weller, private communication and to appear in Proceedings of the 5th International Workshop on Chiral Dynamics, Theory and Experiment (Chiral Dynamics 2006), World Scientific publication, Singapore, 2007, to be published.
- [34] H.J. Arends and S. Scherer, H1 subproject of MAMI funding proposal to DFG, CRC 443 (2008-2010).

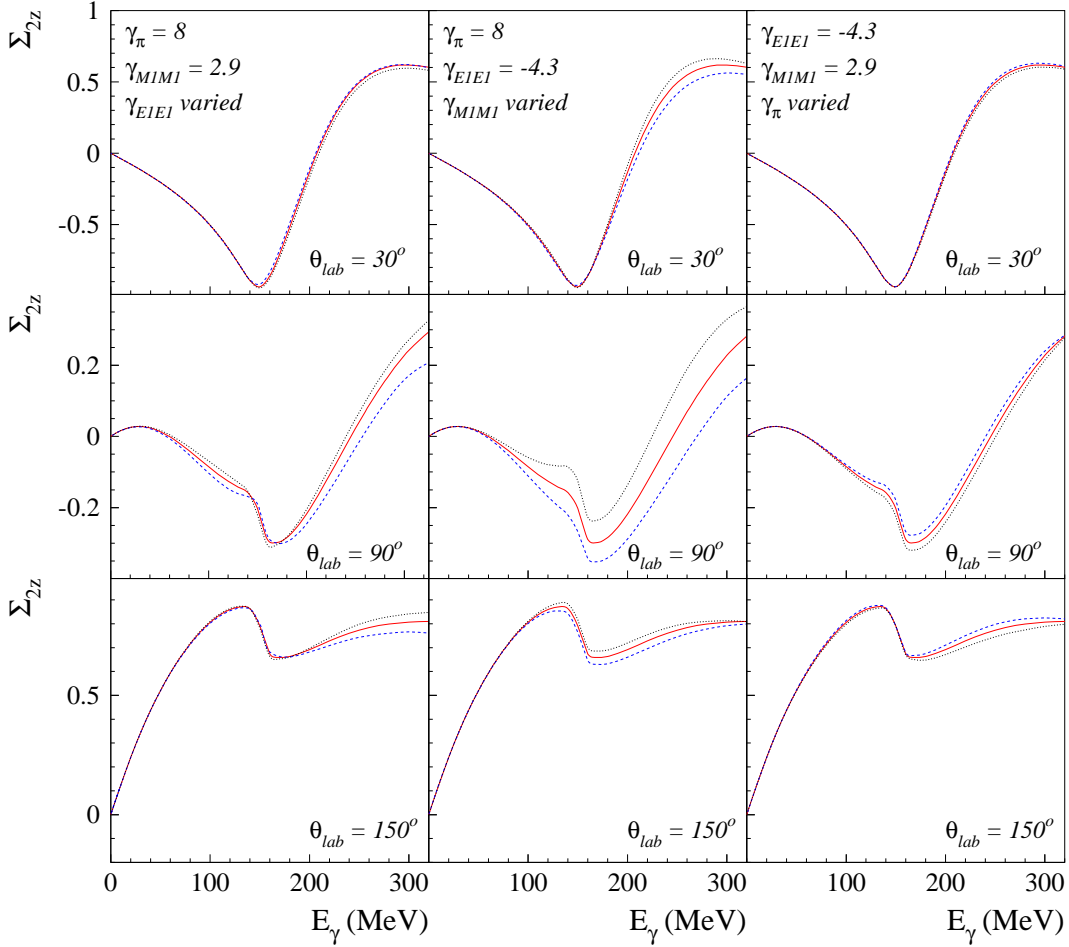


Figure 1: (Color online) The beam-target asymmetry  $\Sigma_{2z}$  as function of the photon lab energy  $E_\gamma$  plotted at different values of the photon scattering angle  $\theta_{lab} = 30^\circ$  (upper row),  $90^\circ$  (central row), and  $150^\circ$  (lower row). The results of the dispersion calculation are obtained by using the experimental values for  $\alpha_{E1}$ ,  $\beta_{M1}$ , and  $\gamma_0$ , as given by Eqs. (18) and (8), while the remaining polarizabilities are taken as free parameters. Left column: results for fixed  $\gamma_{M1M1}$  and  $\gamma_\pi$  as indicated, and the following values of  $\gamma_{E1E1}$ :  $-4.3$  (red solid lines),  $-2.3$  (blue dashed lines), and  $-6.3$  (black dotted lines); central column: results for fixed  $\gamma_{E1E1}$  and  $\gamma_\pi$  as indicated, and the following values of  $\gamma_{M1M1}$ :  $2.9$  (red solid lines),  $4.9$  (blue dashed lines), and  $0.9$  (black dotted lines); right column: results for fixed  $\gamma_{E1E1}$  and  $\gamma_{M1M1}$  as indicated, and the following values of  $\gamma_\pi$ :  $8$  (red solid lines),  $9.8$  (blue dashed lines), and  $7.2$  (black dotted lines).

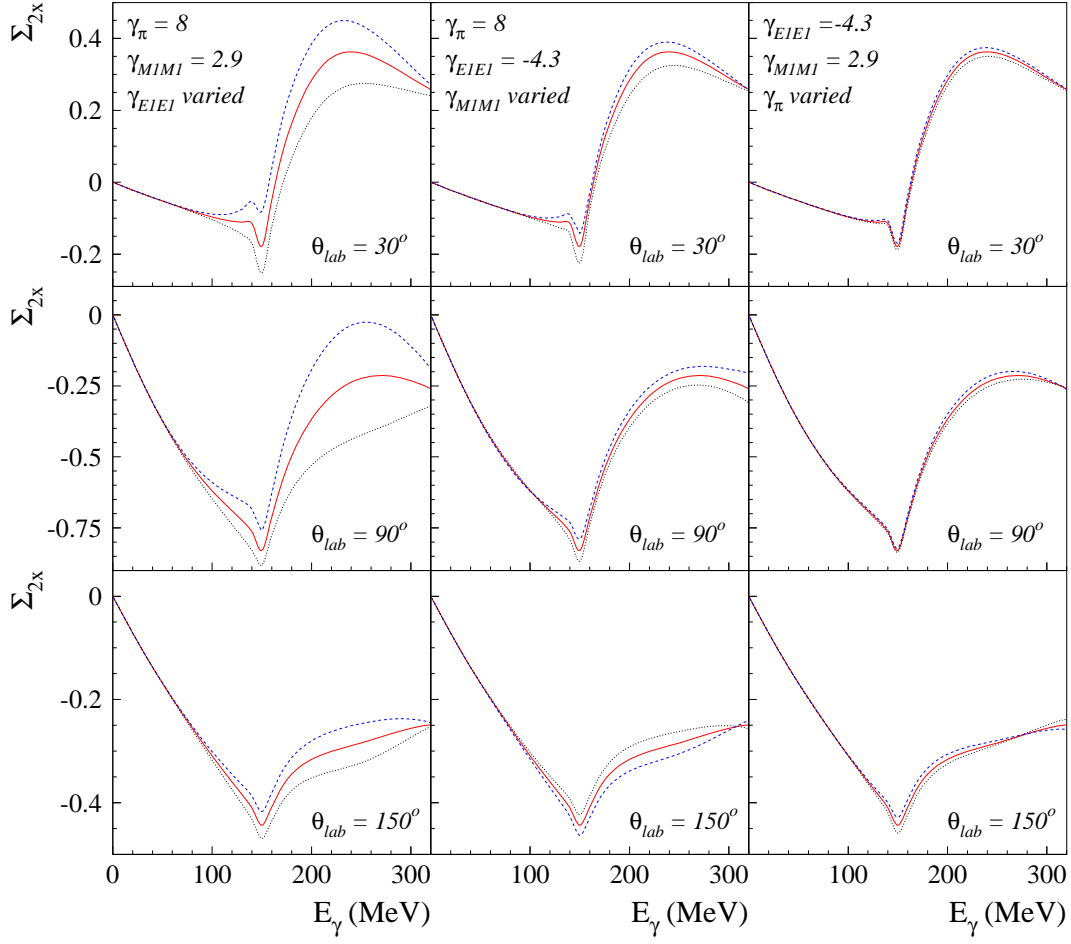


Figure 2: (Color online) The beam-target asymmetry  $\Sigma_{2x}$  as function of the photon lab energy  $E_\gamma$  plotted at different values of the photon scattering angle  $\theta_{lab}$ :  $30^\circ$  (upper row),  $90^\circ$  (central row), and  $150^\circ$  (lower row). For further notation see Fig. 1.

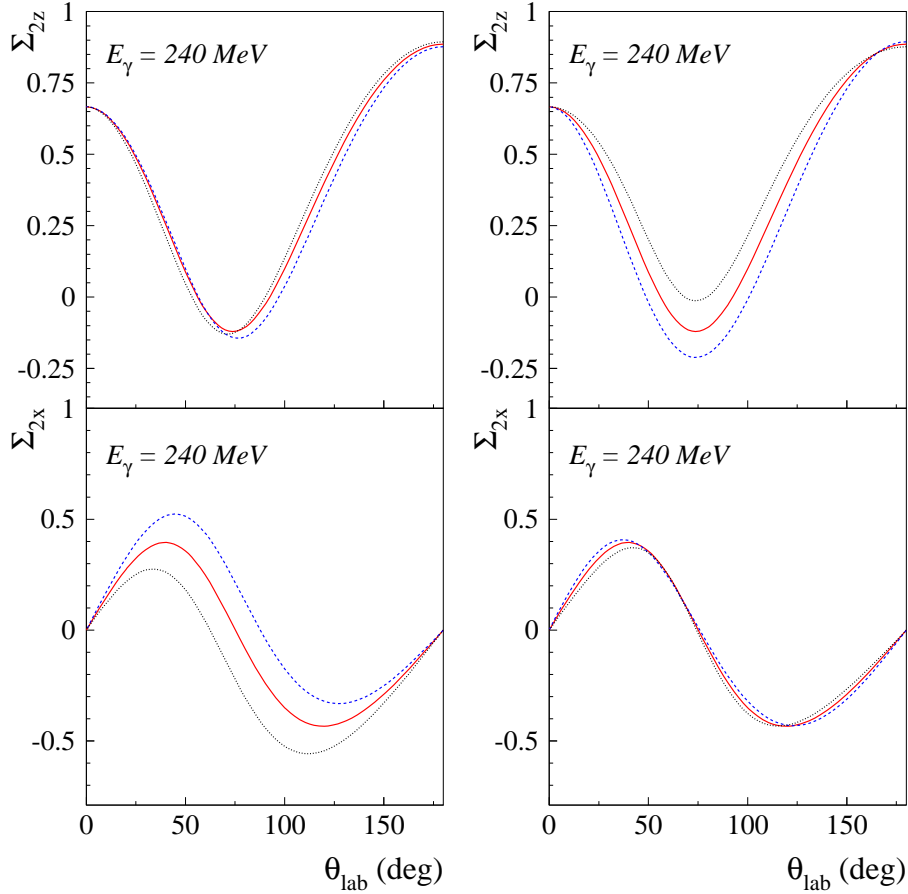


Figure 3: (Color online) The beam-target asymmetries  $\Sigma_{2z}$  (upper row) and  $\Sigma_{2x}$  (lower row) as function of the photon scattering angle  $\theta_{\text{lab}}$  and at fixed photon lab energy  $E_\gamma = 240$  MeV. The results of the dispersion calculation are obtained by using the experimental values for  $\alpha_{E1}$ ,  $\beta_{M1}$ ,  $\gamma_0$ , and  $\gamma_\pi$  as given by Eqs. (18), (9), and (8), while  $\gamma_{E1E1}$  and  $\gamma_{M1M1}$  are taken as free parameters. Left column: results for fixed  $\gamma_{M1M1} = 2.9$  and the following values of  $\gamma_{E1E1}$ :  $-4.3$  (red solid lines),  $-6.3$  (black dotted lines), and  $-2.3$  (blue dashed lines); right column: results for fixed  $\gamma_{E1E1} = -4.3$ , and the following values of  $\gamma_{M1M1}$ :  $2.9$  (red solid lines),  $4.9$  (blue dashed lines), and  $0.9$  (black dotted lines).

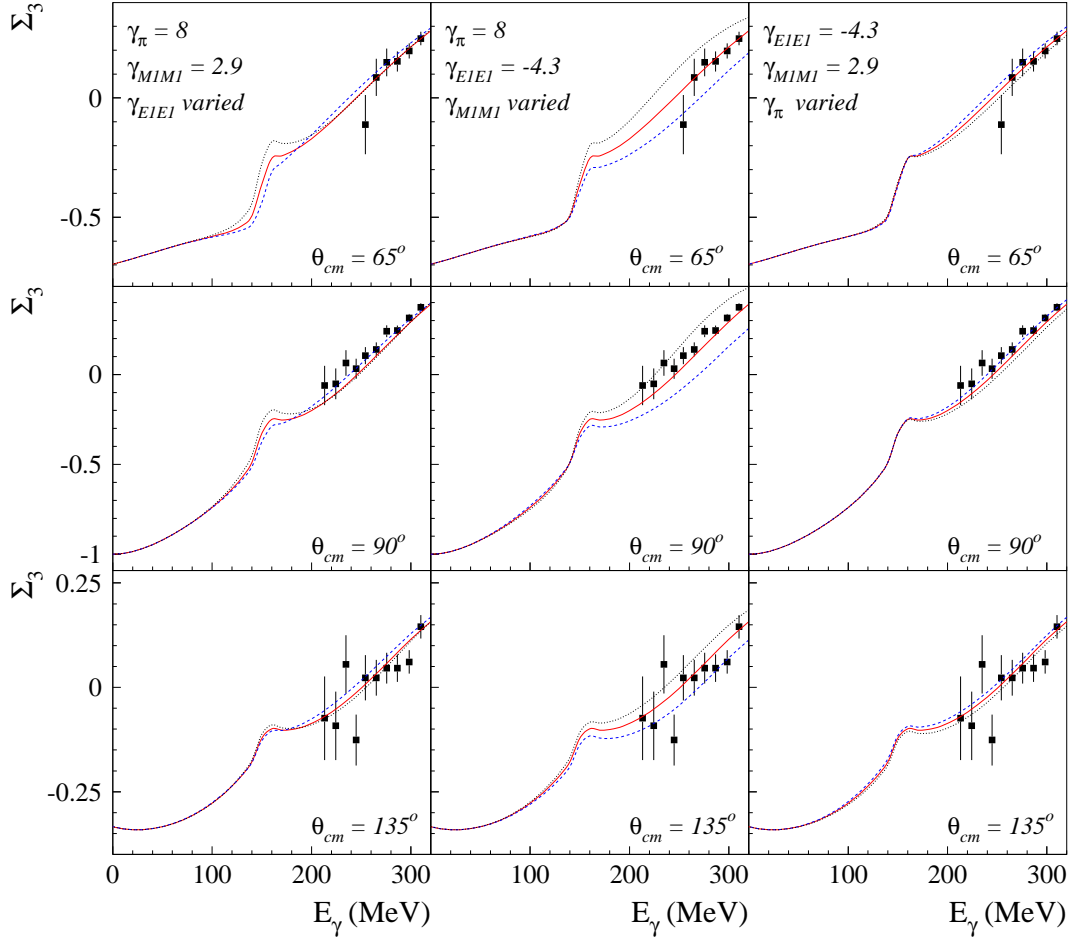


Figure 4: (Color online) The beam asymmetry  $\Sigma_3$  as function of the photon lab energy  $E_\gamma$  plotted at different values of the photon scattering angle  $\theta_{cm}$  :  $65^\circ$  (upper row),  $90^\circ$  (central row), and  $135^\circ$  (lower row). The experimental data are from Ref. [32]. For further notation see Fig. 1.

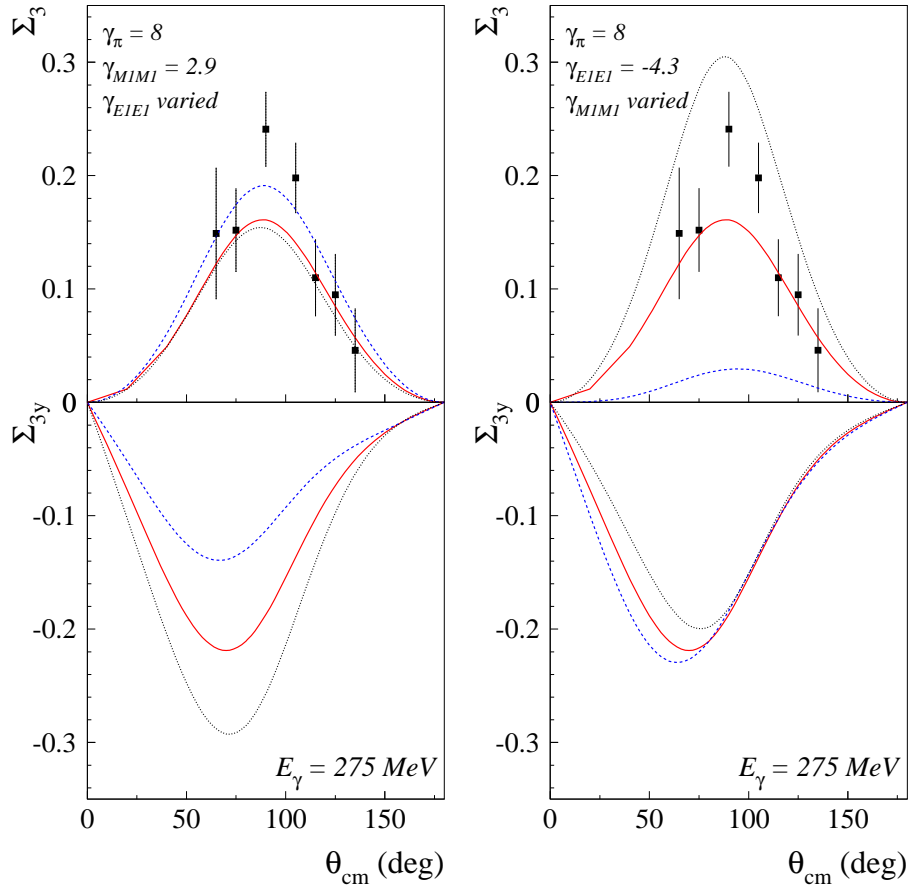


Figure 5: (Color online) The beam asymmetry  $\Sigma_3$  (upper row) and beam-target asymmetry  $\Sigma_{3y}$  (lower row) as function of the photon scattering angle  $\theta_{\text{cm}}$  and at fixed photon lab energy  $E_\gamma = 275$  MeV. The experimental data are from Ref. [32]. For further notation see Fig. 3.



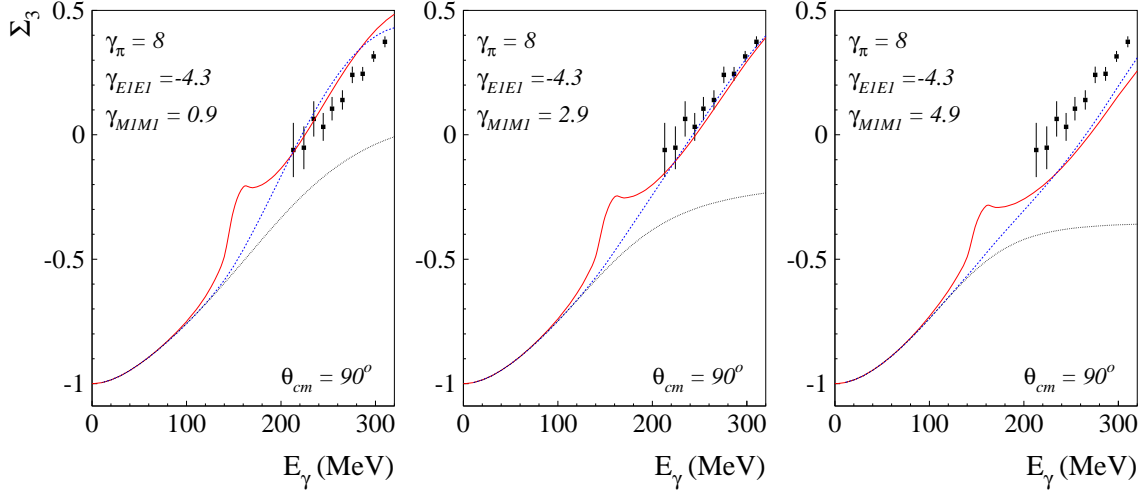


Figure 6: (Color online) Different contributions in the dispersion relation calculation to the beam asymmetry  $\Sigma_3$  as function of the photon lab energy  $E_\gamma$  at photon scattering angle of  $90^\circ$ , for different values of  $\gamma_{M1M1}$  as indicated on the figure. The black dotted curves show the contribution from Born diagrams + subtraction constants +  $t$ -channel. The blue dashed curves are the contribution from Born diagrams + subtraction constants +  $t$ -channel +  $M_{1+}$  multipole in the  $s$ -channel. The red solid curves are the total result. The experimental data are from Ref. [32].

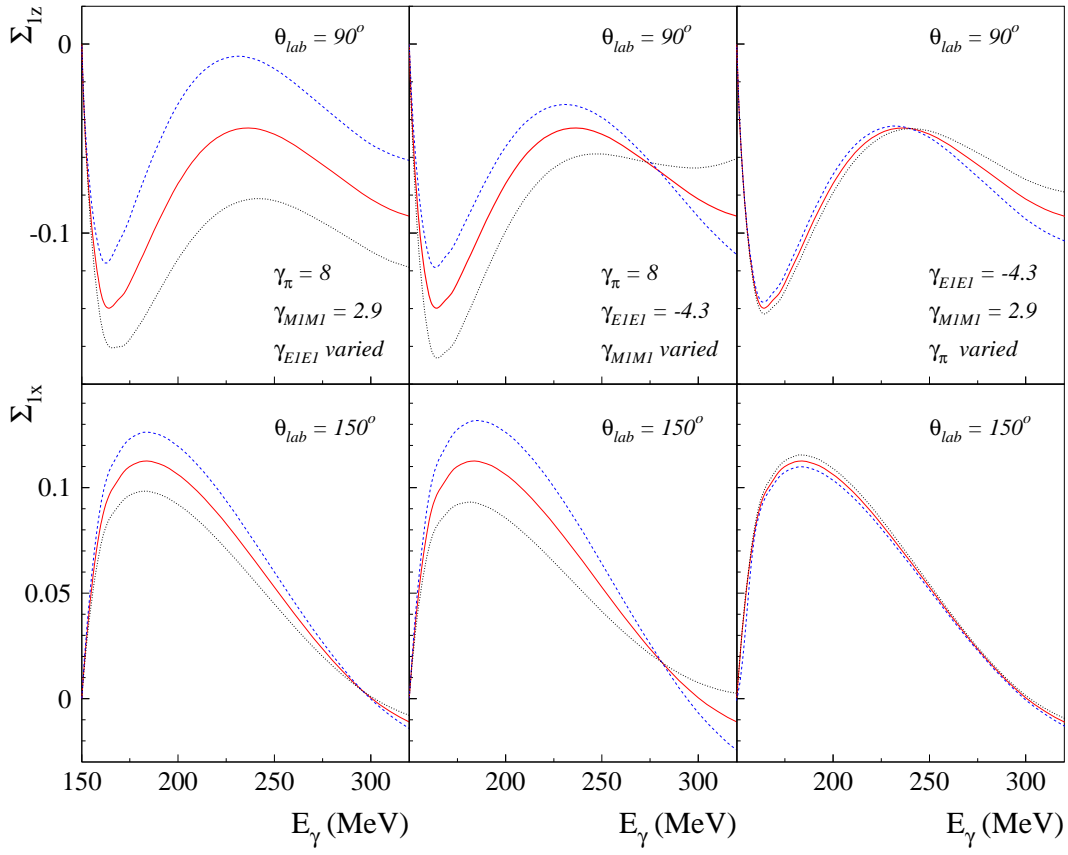


Figure 7: (Color online) The beam-target asymmetries  $\Sigma_{1z}$  (upper row) at photon scattering angle  $\theta_{lab}=90^\circ$  and  $\Sigma_{1x}$  (lower row) at  $\theta_{lab}=150^\circ$ , plotted as function of the photon lab energy  $E_\gamma$ . Further notation as in Fig. 1.